Mon. Not. R. Astron. Soc. **000**, 1–11 (2009) Printed 23 June 2009 (MN LATEX style file v2.2)

Caustics in growing Cold Dark Matter Haloes

Mark Vogelsberger[1⋆], Simon D.M. White[1], Roya Mohayaee[2], Volker Springel[1]
(1) Max-Planck Institut fuer Astrophysik, Karl-Schwarzschild Strasse 1, D-85748 Garching, Germany
(2) Institut d'Astrophysique de Paris (IAP), CNRS, UPMC, 98 bis boulevard Arago, France

Accepted ???. Received ???; in original form ???

ABSTRACT

We simulate the growth of isolated dark matter haloes from self-similar and spherically symmetric initial conditions. Our N-body code integrates the geodesic deviation equation in order to track the streams and caustics associated with *individual* simulation particles. The radial orbit instability causes our haloes to develop major-to-minor axis ratios approaching 10 to 1 in their inner regions. They grow similarly in time and have similar density profiles to the spherical similarity solution, but their detailed structure is very different. The higher dimensionality of the orbits causes their stream and caustic densities to drop much more rapidly than in the similarity solution. This results in a corresponding increase in the number of streams at each point. At 1% of the turnaround radius (corresponding roughly to the Sun's position in the Milky Way) we find of order 10^6 streams in our simulations, as compared to 10^2 in the similarity solution. The number of caustics in the inner halo increases by a factor of several, because a typical orbit has six turning points rather than one, but caustic densities drop by a much larger factor. This reduces the caustic contribution to the annihilation radiation. For the region between 1% and 50% of the turnaround radius, this is 4% of the total in our simulated haloes, as compared to 6.5% in the similarity solution. Caustics contribute much less at smaller radii. These numbers assume a $100\ \mathrm{GeV\ c^{-2}}$ neutralino with present-day velocity dispersion $0.03\ \mathrm{cm\ c^{-1}}$, but reducing the dispersion by ten orders of magnitude only doubles the caustic luminosity. We conclude that caustics will be unobservable in the inner parts of haloes. Only the outermost caustic might potentially be detectable.

Key words: dark matter, caustics, phase-space structure, dynamics, annihilation, N-body

1 INTRODUCTION

Dark matter is thought to consist of weakly interacting particles that are cold, meaning that their thermal velocities in unclustered regions of the present Universe are very small. For example, for standard values of the relevant cross-sections, a neutralino with a mass of $100\ \mathrm{GeV\ c^{-2}}$ is predicted to have a velocity dispersion of just 0.03 cm/s in such regions, corresponding to a very high phase-space density. Since the particles are collisionless, this phase-space density is conserved along particle trajectories, and the nonlinear collapse of dark haloes gives rise to caustics. For infinitely cold dark matter, the density is formally infinite at caustics, because the particles occupy a three-dimensional "sheet" in six-dimensional phase-space and projection of this sheet onto configuration space leads to singularities. These singularities are regularised in realistic cases by the small but finite velocity dispersion of the dark matter particles. These caustics were first discussed by Arnold et al. (1982) and Zel'dovich et al. (1983) for the case of a neutrino-dominated universe. Their properties were worked out in simple, one-dimensional similarity solutions for the growth of spherical haloes by Fillmore & Goldreich (1984) (FG hereafter) and Bertschinger (1985).

It has been suggested that caustics might have an impact on various observables, in particular gravitational lensing (e.g. Gavazzi et al. 2006) or annihilation radiation (e.g. Hogan 2001; Mohayaee et al. 2007; Mohayaee & Salati 2008). Over the last 10 years most studies of the properties of caustics have been based on spherical models for self-similar infall such as those of FG and Bertschinger (1985), or extensions where angular momentum is introduced *ad hoc* to avoid purely radial orbits (White & Zaritsky 1992; Sikivie et al. 1995; Nusser 2001; Natarajan & Sikivie 2006; Natarajan 2007; Sikivie 1998). As we will see below, the original similarity solutions are violently unstable to the radial orbit instability (ROI) (Antonov 1973). Exact density profiles for dark matter caustics were first calculated for the FG model by Mohayaee & Shandarin (2006) (MS hereafter) following an approach originally developed by Zeldovich & Shandarin (1982) and Kotok & Shandarin (1987). In contrast, Hogan (2001) discussed the effect of caustics on annihilation radiation using general arguments which avoid simplified halo models, estimating that caustics might boost the annihilation luminosity by a factor ~ 5 in the outer halo, a significantly larger factor than found by MS for the spherical similarity solution.

⋆ vogelsma@mpa-garching.mpg.de

Although very large simulations of the formation of dark haloes are now feasible (e.g. Diemand et al. 2008; Springel et al. 2008; Zemp et al. 2009), it is still not possible to resolve caustics using standard N-body techniques. Here we use the geodesic deviation equation (GDE) formalism presented in Vogelsberger et al. (2008) (VWHS hereafter) together with a rigorous treatment of caustic passages derived in White & Vogelsberger (2009) (WV hereafter) to follow the evolution of caustics in fully three-dimensional simulations of halo formation. For simplicity, we start from self-similar, spherical initial conditions, but the ROI causes our simulated haloes to develop into highly elongated bars with a detailed structure quite different from that of the spherical similarity solution. This has substantial implications for the number of dark matter streams predicted near the Sun and for the importance of annihilation radiation from caustics.

The plan of our paper is as follows. In Section 2 we describe our initial conditions and the numerical techniques used for our simulations. In Section 3 we demonstrate that our N-body implementation is working correctly by solving a simple spherical test problem. In Section 4 we discuss results from our three-dimensional simulations, contrasting them with the predictions of the similarity solution. We begin with the shape and the density and velocity dispersion profiles, and we move on to fine-grained phase-space structure and the caustic annihilation rate. We give our conclusions in Section 5.

2 NUMERICAL TECHNIQUES

2.1 Initial conditions

We start our simulations from self-similar initial conditions, where most of the particles are in the linear regime, i.e. well beyond the initial turnaround radius. The similarity solutions assume an Einstein-de Sitter universe in which the *linear* mass perturbation δM_i within a sphere containing unperturbed mass M_i, when extrapolated to the initial time $t_{\rm initial}$, satisfies $\delta M_i/M_i = 1.0624(M_i/M_0)^{-\epsilon}$, where ϵ is a scaling index and M_0 is a reference mass taken to be the mass within the turnaround radius at the initial time. The equations of motion for a particle with radial distance r and radial velocity v can then be cast into similarity form by introducing the variables $\lambda = r/r_{\rm ta}$ and $\tau = t/t_{\rm ta}$, where $r_{\rm ta} \propto M_i^{1/3+\epsilon}$ and $t_{\rm ta} \propto M_i^{3\epsilon/2}$ are the turnaround radius and turnaround time of the particle under consideration. The solution $\lambda(\tau)$ of the resulting equation then fully describes the phase-space structure of the halo at all times (see the Appendix and FG for more details on these similarity solutions). Note that the turnaround radius $r_{\rm ta}$ can be viewed either as a function of enclosed mass, as here, or as a function of time, as will often be the case in the following.

We set up our initial conditions in the following way. As a first step we create a uniform gravitational glass within a cubic box with periodic boundary conditions (White 1996). We then cut out the largest sphere contained within the box and use it to represent an unperturbed Einstein-de Sitter universe[1]. We construct similarity initial conditions at time $t_{\rm initial}$ by mapping this uniform distribution $\underline{r}_{\rm glass}$ to the desired initial state by scaling the radial coordinate

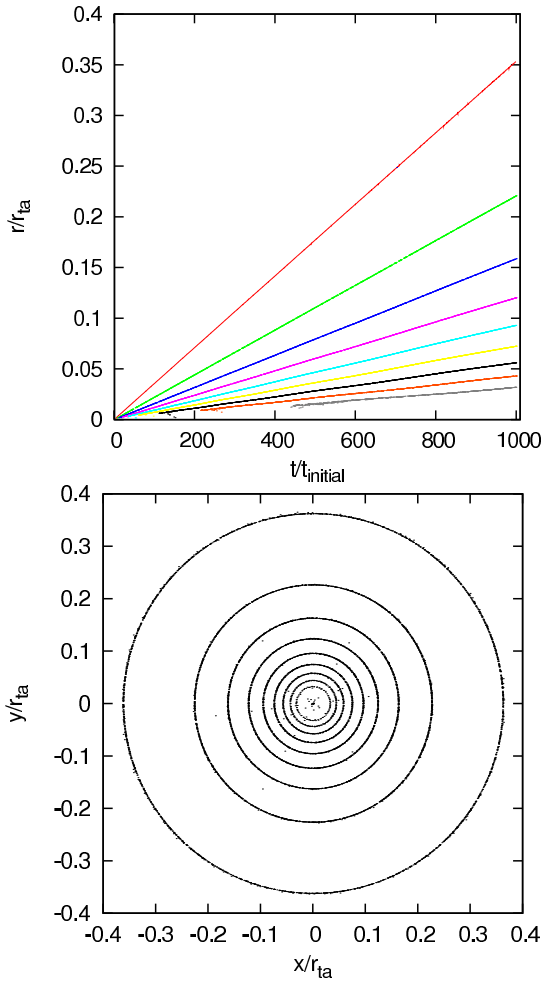

Figure 1. Top panel: Time evolution of the caustic radii in the softened similarity solution ($\epsilon = 2/3$, $\eta = 0.15$) simulated with a (one-dimensional) shellcode. Different colours represent different caustics from red (outermost) to grey (innermost). We note that the softened similarity equation only produces a finite number of caustics while the original FG equations produce an infinite number when approaching the halo centre. The sphere radii grow linearly in time because the turnaround radius increases linearly in time for $\epsilon = 2/3$. Bottom panel: Slice through the caustic spheres. The thickness of the slice is $0.0025\, r_{\rm ta}(t)$. We overlaid all caustics for all times using the similarity scaling. This produces exact spheres (rings in this slice). These plots demonstrate that caustics are tracked correctly over the full simulation period by our GDE method.

and setting velocities according to the similarity solution $\lambda(\tau)$

$$\underline{r}(t_{\rm initial}) = r_{\rm ta}(M_0)\, \frac{\lambda(\tau)}{\tau^{2/3+2/(9\epsilon)}}\, \frac{\underline{r}_{\rm glass}}{r_{\rm glass}},$$
$$\underline{v}(t_{\rm initial}) = \frac{r_{\rm ta}(M_0)}{t_{\rm initial}}\, \frac{{\rm d}\lambda/{\rm d}\tau}{\tau^{-1/3+2/(9\epsilon)}}\, \frac{\underline{r}_{\rm glass}}{r_{\rm glass}}, \qquad (1)$$

where the similarity time variable τ is determined from the enclosed mass according to $\tau = (M_i/M_0)^{-3\epsilon/2}$.

We run our simulations from $t_{\rm initial}$ to $t_0 = 2/(3\ H_0) \cong 9.1$ Gyr, where we adopt $H_0 = 72\ {\rm km\ s^{-1}\ Mpc^{-1}}$ as the Hubble constant today. If we require that the turnaround of the bounding sphere occurs at t_0, choosing the scaling index ϵ and the mass fraction $M_0/M_{\rm tot}$ within the initial turnaround radius determines the initial time as $t_{\rm initial} = t_0(M_0/M_{\rm tot})^{3\epsilon/2}$ and defines a unique mapping from the uniform spherical glass to the similarity solution

[1] Note that this cut means that a cubic glass with N^3 particles will produce a sphere with $N^3/(6/\pi) \cong N^3/2$ particles. In the following we will always specify the resolution of our simulations by giving the number of particles in the original cube.

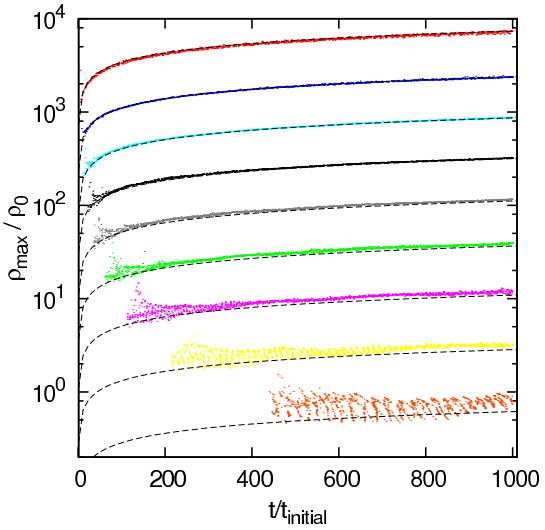

Figure 2. Maximum caustic densities in units of the stream density at turnaround ρ_0. Black dashed lines show maximum densities for the analytic solution. The densities increase with time, because the velocity dispersion $\sigma_{\rm b}$ decreases with time.

at $t_{\rm initial}$. In the following we will always use this kind of initial conditions.

2.2 Simulation code

For our simulations we adapt the GADGET-3 code that was developed originally for the Aquarius project (Springel et al. 2008). We apply vacuum boundary conditions, use (unless otherwise noted) a spline softening kernel with constant smoothing length in comoving coordinates ($\propto t^{2/3}$ in an Einstein-de Sitter universe), and run our simulations in physical coordinates. We modified the code to integrate the GDE as described in VWHS and to track radiation from each particle due to annihilations within its own fine-grained phase-space stream, as described in WV. This automatically accounts for the enhanced radiation as particles pass through caustics. We set the GADGET force accuracy parameter to 10^{-4} and chose a time integration accuracy of 10^{-3} (see Springel 2005, for the significance of these terms). We checked that these settings are sufficient to produce reliable results.

To gain performance and accuracy we integrate the GDE directly for each particle only after it has passed through turnaround. At turnaround all variables related to the fine-grained phase-space density are set to the values predicted by the analytic FG solution. We implement this by checking in each drift operation whether a given particle is currently turning around and initialising the integration of the phase-space distortion tensor when this is the case. We demonstrate below that using the analytic solution until turnaround is well-justified. As a particle turns around at $t_{\rm ta}$, its phase-space distortion tensor is set to unity and its stream density, i.e. the local 3-density of the particular stream in which it lives, is set to the dark matter density of the similarity solution at the turnaround point $\rho_0 = 9\pi^2/(16(3\epsilon+1))\ \rho_{\rm b}(t_{\rm ta})$, where $\rho_{\rm b}(t_{\rm ta}) = 1/(6\pi G t_{\rm ta}^2)$ is the mean density of the Einstein-de Sitter background at time $t_{\rm ta}$. The (fine-grained) dark matter velocity dispersion σ_0 at that time and position can be calculated using conservation of phase-space density $\rho_0/\sigma_0^3 = \rho_{\rm b}(t_0)/\sigma_{\rm b}(t_0)^3$, where $\sigma_{\rm b}(t_0)$ is the dark matter velocity dispersion predicted for unclustered matter today. For a neutralino of mass m_p we have $\sigma_{\rm b}(t_0) \sim 10^{-11}{\rm c}\ ({\rm GeV\ c^{-2}}/m_p)^{1/2}$. Unless otherwise noted, we will assume a 100 GeV c^{-2} neutralino, resulting in $\sigma_{\rm b}(t_0) = 0.03$ cm/s. Finally, the sheet orientation at turnaround is set to

$$V_{q,ij} = \frac{{\rm d}V_i(q)}{{\rm d}q_j} = \frac{x_i x_j}{r^2}\left(\frac{3\pi}{4}\right)^2 \frac{1}{3+1/\epsilon}\frac{1}{t_{\rm ta}}, \qquad (2)$$

where $V_i(q)$ are the three components of the initial cold dark matter sheet (see VWHS and WV). All GDE simulations presented in this paper have the fine-grained phase-space quantities initialised for each particle at turnaround in this way.

3 RESULTS

3.1 Embedded 1D tests

To test the GDE implementation in GADGET-3 it is desirable to have a system where we can analytically evaluate the fine-grained phase-space structure. This is straightforward for the FG similarity solution (see the Appendix for details). Starting with the initial conditions described above we might expect to be able to reproduce the similarity solution with our code. This is not possible, however, because the FG solution is violently unstable to both radial and non-radial perturbations, as we show below. Although this result does not appear to have been demonstrated before for the specific case of the FG solution, it is expected given earlier work on other spherical collapse models. This has found instabilities not only in the fully 3-dimensional case where the radial orbit instability (ROI) turns the system into a highly elongated bar (e.g. Antonov 1973; Polyachenko 1981; Barnes 1985; Carpintero & Muzzio 1995; Merritt 1999; MacMillan et al. 2006; Bellovary et al. 2008), but also in 1D (i.e. enforcing spherical symmetry and radial orbits) where the regular phase-space pattern of the similarity solution still gets destroyed (Henriksen & Widrow 1997, 1999). These instabilities have a dramatic impact on the fine-grained phase-space structure as we will show below, so we cannot follow this route to check our standard code against the known similarity solution.

A test can nevertheless be carried out by keeping the calculation *artificially* stable. It turns out that the following approach works. We replaced the GADGET-3 treecode by a shellcode, where radial forces are calculated based purely on the enclosed mass. Particles in the initial conditions then represent mass shells. This removes the degree of freedom exploited by the ROI, but does not stabilise the system against purely 1-D instabilities. To avoid the destruction of the similarity phase-space pattern, we must in addition soften quite strongly the gravitational potential. One can show that a Plummer-softening that scales with the turnaround radius still allows a similarity solution. The similarity equation is then a slight extension to the FG equation

$$\frac{{\rm d}^2\lambda}{{\rm d}\tau^2} = -\frac{2}{9}\left(\frac{3\pi}{4}\right)^2 \tau^{2/(3\epsilon)} \frac{\lambda}{(\lambda^2+(\eta\Lambda)^2)^{3/2}} \mathcal{M}\left(\frac{\lambda}{\Lambda}\right), \qquad (3)$$

where $\mathcal{M}$ is the dimensionless enclosed mass

$$\mathcal{M}\left(\frac{\lambda}{\Lambda}\right) = \frac{2}{3\epsilon}\int_1^\infty \frac{{\rm d}\xi}{\xi^{1+2/(3\epsilon)}} \mathcal{H}\left[\frac{\lambda}{\Lambda} - \frac{\lambda(\xi)}{\Lambda(\xi)}\right], \qquad (4)$$

$\mathcal{H}$ the Heaviside function, $\Lambda(\tau) = \tau^{2/3+2/(9\epsilon)}$ and η is the Plummer-softening length in units of the turnaround radius. We can solve this softened similarity equation in the same way as the original FG equation, including the parallel GDE integration as described in the appendix. With this setup we can check our N-body

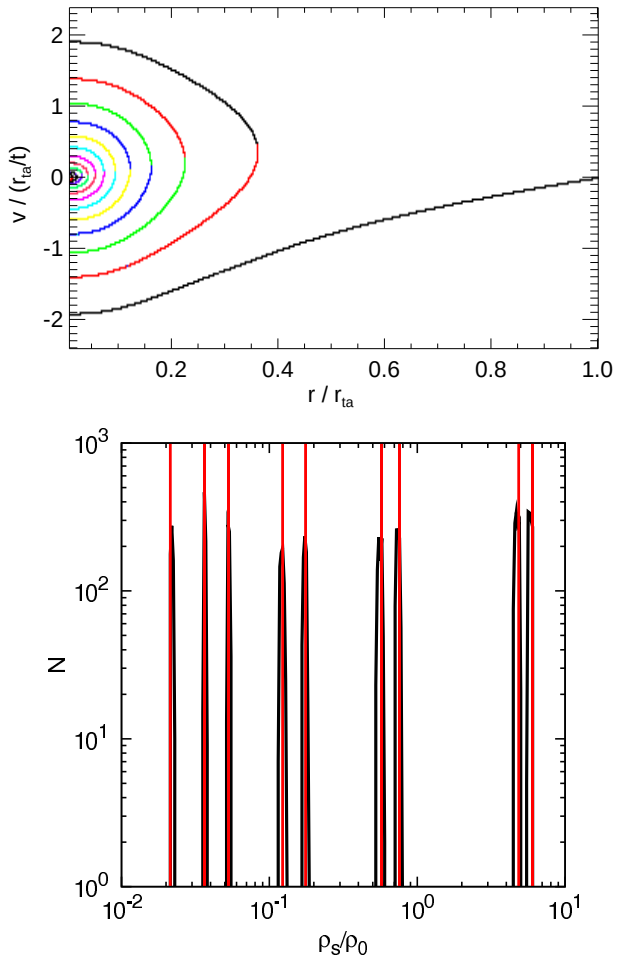

Figure 3. Top panel: Phase-space portrait at t_0 for the softened similarity system. The various colours indicate how many caustics each particle has passed. Infalling particles have seen no caustic (black line). They go through the centre, and move out to the first apocentre, where they pass the outermost caustic. The colour changes to red at this point and stays red until the second caustic is reached, and so on. We note that the softened similarity solution has only a finite number of caustics. This is why the phase-space is not densely occupied at low $r/r_{\rm ta}$ as in the case for the original unsoftened FG solution. Bottom panel: Densities of individual dark matter streams in the interval $r/r_{\rm ta} \in (0.1, 0.105)$. At this distance the portrait shows nine streams (the innermost stream is coloured in yellow and particles belonging to it have passed four caustics). In black we show a histogram of their densities in the GDE simulation and in red the analytically predicted stream densities. The agreement is good, demonstrating that our method can correctly recover the density of individual streams.

implementation by comparing the results to the analytic solution of the softened similarity equation.

The following results are based on a $N = 128^3$ simulation with this method. We have chosen $\epsilon = 2/3$, $r_{\rm ta}(t_0) = 1400$ kpc, $t_{\rm initial} = t_0/10^3$ and $\eta = 0.15$, where $r_{\rm ta}$ denotes the global turnaround radius of the halo.

Fig. 1 shows how well our code reproduces the caustic structure of this test problem. The top panel shows the time evolution of the caustic radii. They grow linearly in time, because the turnaround radius is proportional to t for $\epsilon = 2/3$. The different colours represent the different caustic spheres (red is the outermost sphere, green the second, and so on). We note that the softened FG equation has only a finite number of caustics for large η (nine for $\eta = 0.15$) while the original FG solution (the $\eta \to 0$ limit) produces an infinite number of caustics. The bottom panel shows a slice through the caustic spheres from a wide range of times after scaling each to its own turnaround radius. In this plot we thus overlay the complete time evolution of the system. One can clearly see that the caustics build perfect spheres that scale exactly as expected.

The maximum densities in these caustics are shown in Fig. 2. The agreement of the GADGET-3 shellcode results with the analytic solution (black dashed lines) is good. The maximum density $\rho_{\rm max}/\rho_0$ is proportional to $1/\sqrt{\sigma_b(t)}$ for $\epsilon = 2/3$, and therefore increases with time due to the decrease of the velocity dispersion.

In Fig. 3 we focus on the density of individual fine-grained dark matter streams. We determine the density of individual streams by binning $\rho_{s,i}/\rho_{0,i}$ for all particles i in $r/r_{\rm ta} \in (0.1, 0.105)$, where $\rho_{s,i}$ is the density of the stream particle i is embedded in and $\rho_{0,i}$ is its stream density at turnaround. From the phase-space portrait Fig. 3 (top panel) one can see that there are 9 distinct streams in this radial interval. In the bottom panel we show the resulting stream density histogram in black. In red we overplot the analytic result for the densities of the nine streams. The agreement is good, showing that we correctly recover the density of individual streams in this system.

We will now briefly described how we calculate the intra-stream annihilation rate for each individual simulation particle, that is the annihilation rate due to encounters with other particles in its own DM stream (see VWHS, WV). Each simulation particle (mass m_i) represents many dark matter particles (mass m_p). The intra-stream annihilation rate of one dark matter particle is given by $(\langle\sigma_A v\rangle/m_p)\rho_{s,i}$. Therefore, the annihilation rate of a simulation particle is given by $(\langle\sigma_A v\rangle/m_p^2)(\rho_{s,i} m_i)$. To get an estimate of the intra-stream annihilation rate, we integrate the stream density along the trajectories of all particles as the simulation is run. This yields for every particle and at each snapshot time t_k the time-integrated rate

$$A_i(t_k) = \int_{t_{\rm initial}}^{t_k} {\rm d}t \;\; \rho_{s,i}(t), \tag{5}$$

where we set the particle physics prefactor $\langle\sigma_A v\rangle/m_p^2$ to unity. When passing through a caustic it is necessary to calculate the time integral analytically as described in WV, since the simulation time-stepping is usually not fine enough. Based on $A_i(t_k)$ and $A_i(t_l)$ $(t_k < t_l)$ we can calculate the intra-stream annihilation rate of particle i

$$\langle P_i\rangle_{\rm intra} = m_i \, \frac{A_i(t_l) - A_i(t_k)}{\Delta t}. \tag{6}$$

In the following we apply this scheme to calculate the intra-stream annihilation rate of individual particles.

3.2 3D results

In this section we study halo formation from the same initial conditions as above, but with fully 3D gravity. Thus we replace the 1D shellcode of the last section with our modified version of the tree-code GADGET-3. In addition, we choose a much smaller softening. The ROI then acts with full force and the system develops a highly elongated bar in its inner regions. Our goal here is to study how this more complicated dynamical structure affects the fine-grained phase-space of the system, and what implications this has for the intra-stream annihilation rate. In the following we use a $N = 128^3$

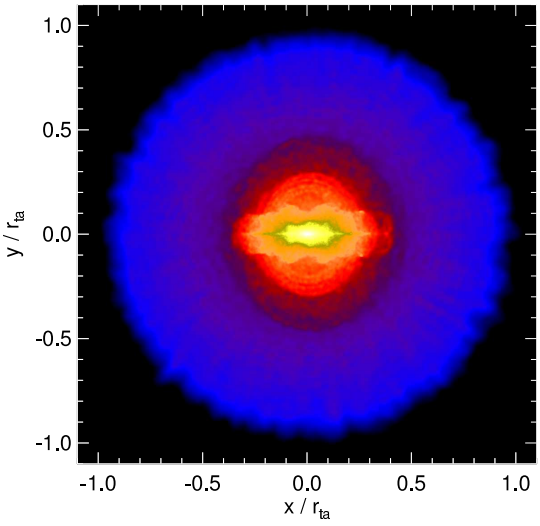

Figure 4. Projected density of a slice of thickness $0.25r_{\rm ta}$ through the 3D simulation at the final time when $r_{\rm ta}$ equals the radius of of the entire simulated region. The strong bar is clearly visible and is oriented to lie in the plane of the slice. It formed through the action of the ROI. The red region is bounded by the outermost caustic.

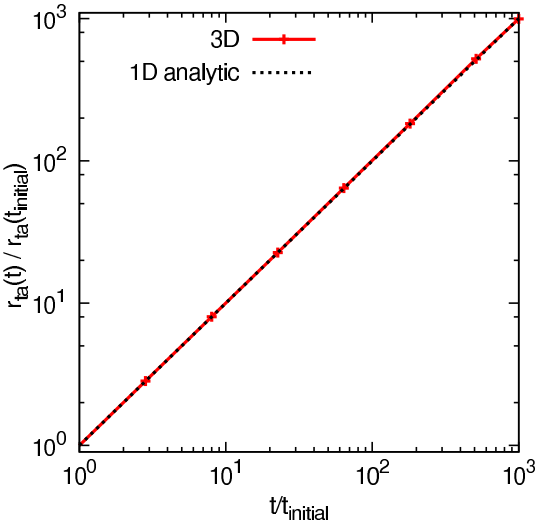

Figure 5. The turnaround radius evolution of the 3D simulation is compared to the expectation from the 1D analytic similarity solution. Although the structure of the 3D halo is very different from that of the similarity solution, the turnaround radius grows in exactly the same way, linearly in time for $\epsilon = 2/3$.

simulation with a comoving softening length of $0.01\ r_{\rm ta}(t_0)$. We checked that our results do not depend on resolution (either particle number or softening) in any significant way.

In Fig. 4 we show the projected density of a slice through the centre of the halo at t_0 with a thickness of $0.25\ r_{\rm ta}(t_0)$. At this time the last simulation particles are just reaching turnaround. The blue region marks the halo beyond the outermost caustic, hence the one-stream regime. The change to red marks the region of multiple streams. The occupied region has a sharp spherical edge at $r_{\rm ta}$, showing that the influence of our vacuum boundary condition has not propagated into the inner regions of interest. We checked this explicitly with other simulations, and also by verifying that the results given below are very similar to those at $0.5t_0$ once these are scaled up according to the similarity scaling. Clearly visible in Fig. 4 is a strong bar produced by the ROI. To show it optimally, we have oriented our slice perpendicular to its minor axis. At the time, shown we estimate axis ratios $b/a = 0.41$ and $c/a = 0.22$ from the moment of inertia of all particles within $r_{\rm ta}$, axis ratios $b/a = 0.34$ and $c/a = 0.17$ from all particles within $0.5\ r_{\rm ta}$, and $b/a = 0.28$ and $c/a = 0.12$ from those within $0.1\ r_{\rm ta}$. These numbers are quite similar at $t = 0.5t_0$ suggesting that the system is evolving in a nearly self-similar, though non-spherical fashion.

Although the inner structure of the halo is very different from the FG model, the turnaround radius grows in time just as this model predicts. This is demonstrated in Fig. 5, where the dashed black line is the FG prediction for $\epsilon = 2/3$. This behaviour is expected since the growth of the turnaround radius depends on the monopole term in the halo mass distribution and this is not affected by non-spherical contributions from the inner part. We note that this is important for our GDE integrations because we use the analytic FG solution to initialise the GDE variables at the turnaround radius.

It is obvious that the strong departures from spherical symmetry must nevertheless substantially change the structure of the system. The changes are less dramatic than might be expected, however. In Fig. 6 we plot the spherically averaged density profile as a function of radius at t_0 both for the 3D simulation and for the similarity solution. Except for the caustic spikes, the mean halo density profile in agrees very well over most of the plotted radial range with the similarity prediction. The deviations visible on the smallest scales in Fig. 6 are an effect of force softening. We have performed simulations with 20 times smaller softening, finding that the spherically averaged profile does not deviate significantly from isothermal form ($\rho \propto r^{-2}$) down to $10^{-3}\ r_{\rm ta}$. We have also checked that if we change the value of the similarity exponent ϵ in our initial conditions, the inner profiles of the resulting bar-like haloes are always well described by a power law with exponent $9\epsilon/(1+3\epsilon)$, the value predicted by spherical similarity solutions with nonradial orbits (White & Zaritsky 1992; Sikivie et al. 1995; Nusser 2001).

The ROI disturbs the overall radial structure of the system very little. We see no sign of a tendency to drive the system towards a "universal" NFW-like profile of the kind which MacMillan et al. (2006) and Bellovary et al. (2008) found in their own experiments from non-similarity initial conditions. This demonstrates that the ROI does not of itself produce NFW structure, though it may, of course, be acting in concert with other processes in these earlier experiments.

The aspherical structure of the inner regions induces nonradial motions in the infalling material, producing a phase-space distribution which is six-dimensional rather than two-dimensional as in the similarity solution. We illustrate how this affects the velocity dispersion structure in Fig. 7. The upper panel shows total and radial velocity dispersions (relative to mean radial streaming) as functions of radius in units of $r_{\rm ta}$, while the lower panel is a similar plot for the velocity anisotropy parameter $\beta(r)$. In both panels the 3D simulation result (which is at t_0) is compared with the spherical similarity solution. The total velocity dispersion of our 3D halo tracks that in the similarity solution quite accurately down to $0.04r_{\rm ta}$, once the features due to the spherical caustics in the latter are smoothed over. At smaller radii it turns over and drops significantly. This reinforces the conclusion from Fig. 6 that the coarse-grained structure of our simulated halo is similar to that of the similarity solution despite their difference in shape. While at $r > 0.05r_{\rm ta}$ orbits in our bar-like halo are predominantly radial and so resemble those in the FG similarity solution, at smaller radii

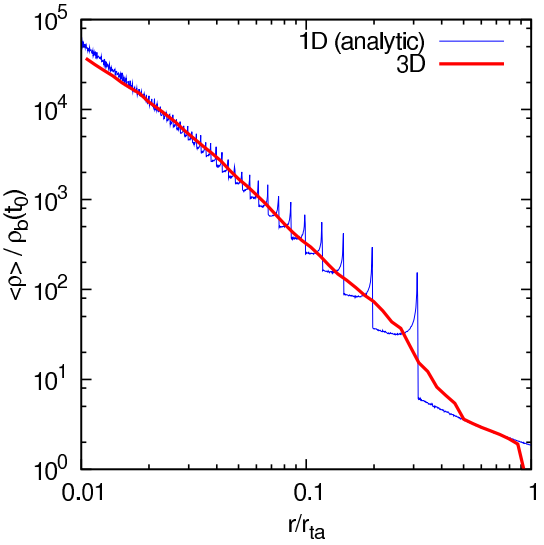

Figure 6. Spherically averaged density profile of the 3D simulation compared to the FG similarity solution. Apart from the clear caustic spikes in the 1D case, the two density profiles agree very well despite the very large shape difference between the corresponding objects. The small deviation at $r < 0.015 r_{\rm ta}$ is due to the softening of the simulation.

the velocity distribution becomes much closer to isotropic and the radial velocity dispersion begins to decline towards the centre.

The ROI leads to a considerably more complex fine-grained phase-space pattern in our 3D simulation than in the FG similarity solution. Phase-space is two-dimensional in the latter, with the particles occupying a one-dimensional subspace which is fixed in similarity variables. In contrast, phase-space is six-dimensional in our simulation, with the particles occupying a heavily wrapped three-dimensional subspace. When this subspace is projected onto the two-dimensional phase-space of the similarity solution, the fact that the particles occupy a low-dimensional subspace is no longer evident. We show this explicitly in Fig. 8, where the pattern of the 1D similarity solution (the grey lines) is compared to the projected particle distribution at t_0 in our simulation. The colours in the 3D case mark the number of caustics each particle has passed. As in the 1D case, this number increases towards the centre, because of the shorter orbital periods at smaller radii. Near and beyond the turnaround radius particles follow the similarity solution, but deviations are already visible at $r \sim 0.5\, r_{\rm ta}$, where the infalling particles no longer lie exactly on the analytic sheet.

The increase in dimensionality of the phase-space distribution has a dramatic effect on the density of individual dark matter streams. Away from caustics the stream density surrounding a particular particle is expected to decrease from its value at turnaround in proportion to $(t/t_{\rm ta})^{-1}$ for an effectively one-dimensional system like the similarity solution, but in proportion to $(t/t_{\rm ta})^{-3}$ for a three-dimensional system like our simulation (Helmi & White 1999, and VWHS) . In Fig. 9 we show the median of the normed stream density (i.e. the stream density relative to its value at turnaround) for particles in radial bins at $t = t_0$, again comparing results for the simulation and for the 1D similarity solution. Beyond the outermost caustic, stream densities are very similar in the two cases. At smaller radii the stream density dilution increases much faster towards the centre in the simulation than in the similarity solution. In the former case the inner behaviour is very close to a power-law. (Recall that for both models the typical orbital period at

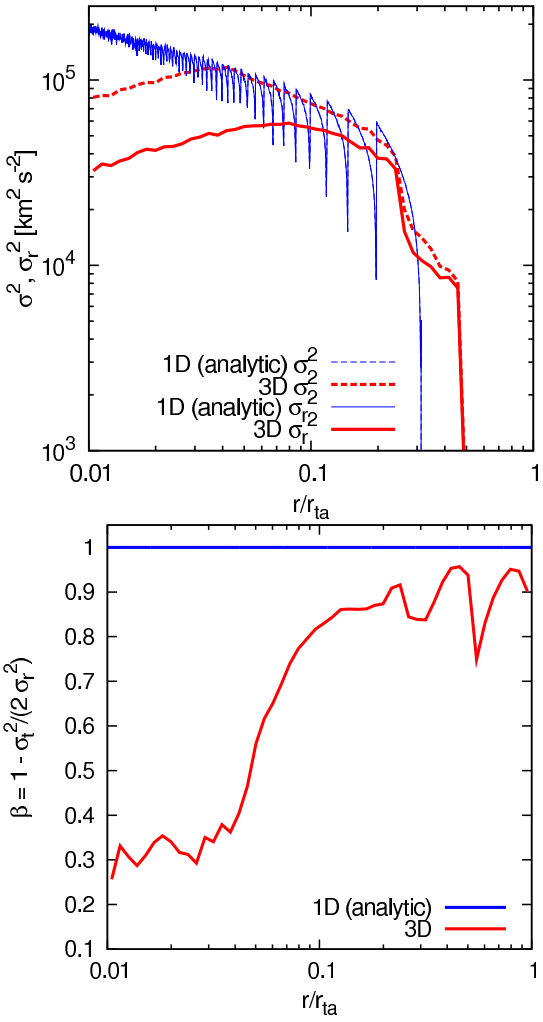

Figure 7. Top panel: Total ($\sigma^2 = \sigma_r^2 + \sigma_t^2$, where σ_r and σ_t are the velocity dispersions in the radial and tangential directions, respectively) and radial (σ_r^2) velocity dispersion profiles for the 3D halo are compared to the radial velocity dispersion profile of the FG similarity solution. Bottom panel: Velocity anisotropy profile $\beta = 1 - \sigma_t^2/(2\sigma_r^2)$. Apart from caustic features the total velocity dispersion behaviour is very similar in the two models for $r > 0.04 r_{\rm ta}$. In the outer part of the halo, orbits are primarily radial ($\beta \sim 1$), but the velocity distribution becomes more nearly isotropic for $r < 0.05 r_{\rm ta}$ and this causes both dispersions to drop in the inner regions as in spherical similarity solutions with nonradial orbits.

each radius is roughly proportional to radius, so a power law close to r^1 is expected in the 1D case.) In the simulation the variation of dilution with radius is less smooth, but is still moderately well represented by a power-law which, as expected, is the cube of the one which best fits the similarity solution.

Fig. 10 presents the radial variation of stream density in a slightly different way. The stream density associated with each particle is here divided by the current mean density of the Universe, rather than by its value at turnaround. The plot is then constructed by taking medians in 50 equal logarithmic bins in radius, just as in Fig. 9. In the 1D similarity solution, stream densities increase quite strongly (approximately as r^{-1}) towards the centre, because the dilution effect seen in Fig. 9 is more than compensated by the fact that particles near the centre typically turned around earlier, and so had higher stream densities at turnaround. For the 3D simulation, on the other hand, the much stronger dilution towards the

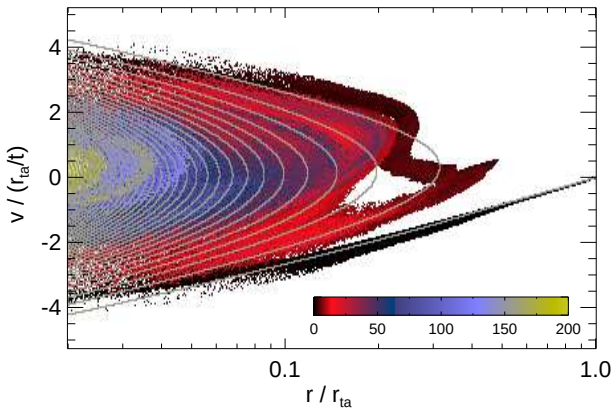

Figure 8. Phase-space portrait at t_0 for the 3D simulation and (overplotted in grey) for the 1D similarity solution for $\epsilon = 2/3$. The ROI destroys the clear phase-space pattern seen in the similarity solution. The coarse shape in the two cases is similar, but the 3D solution does not have a simple fine-grained structure in this particular projection of its 6-dimensional phase-space. For the 3D solution the colours encode the number of caustics a given particle has passed (see colourbar). One can clearly see that this grows towards the centre, exceeding 200 in the innermost regions.

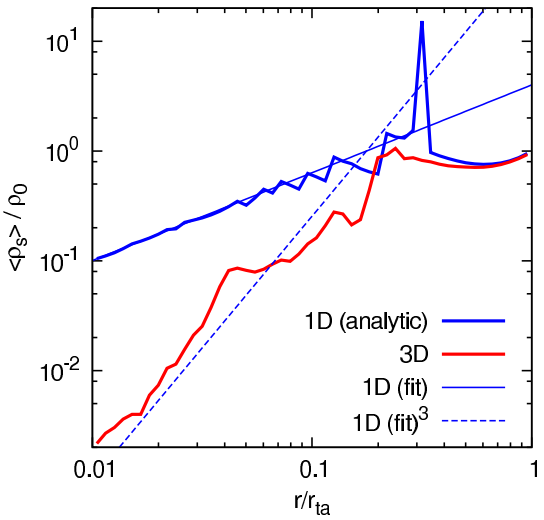

Figure 9. Median normed stream density (i.e. the stream density surrounding each particle in units of its value at turnaround) for the 1D similarity solution (the thick blue line) and for the fully 3D simulation (the thick red line). The 1D relation was calculated from the exact (non-softened) similarity solution for $\epsilon = 2/3$. Due to the fully three-dimensional structure of the orbits, stream densities are diluted much faster towards the centre in the simulation than in the similarity solution. In both cases the median was calculated for 50 equal logarithmic bins in radius. This smooths out the caustics of the 1D solution except for the outermost few. The thin blue line is a power-law fit $\rho_s \propto r^{0.8}$ to the normed stream density in the inner part of the similarity solution. The blue dashed line is proportional to the 1D density dilution to the power of three and, as expected, agrees fairly well with the stream dilution in the inner regions of the 3D simulation.

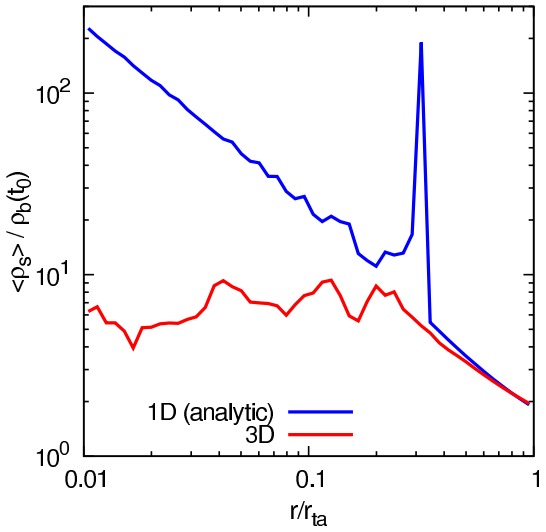

Figure 10. The median stream density in units of the current cosmic mean density of the particles in each of 50 logarithmic bins in radius at time t_0. Results are shown for the 1D similarity solution (blue) and for the 3D simulation (red). While the stream density increases towards the centre for the similarity solution, it is almost constant with radius in the simulation.

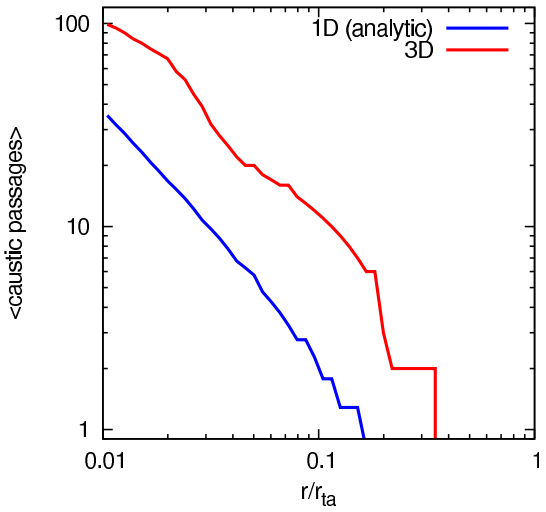

Figure 11. Median number of caustic passages experienced by particles in a set of logarithmic bins in radius. The result for the 1D similarity solution is shown as a solid blue line, that for the 3D simulation in red. As expected due to the more complex orbit structure, the number of caustics at a given radius increases by about a factor of three from 1D to 3D. The bump near $r/r_{\rm ta} = 0.1$ is related to the complex feature in phase-space seen in Fig. 8.

centre results in typical stream densities which are approximately constant with radius at any given time. Note that both in this figure and in the last, medians are taken over the stream density distribution of the particles in each radial bin. Thus they give the stream density value that splits the *mass* at each radius in half. As we will see below, this is much larger than the density of a *typical* stream at that radius.

Typical stream densities are quite similar near the outermost caustics in the 1D similarity solution and in the 3D simulation, but they become very different in the inner regions. In contrast, the typical number of caustics varies with radius in the same way in the two cases. This can be seen in Fig. 11, where we plot the me-

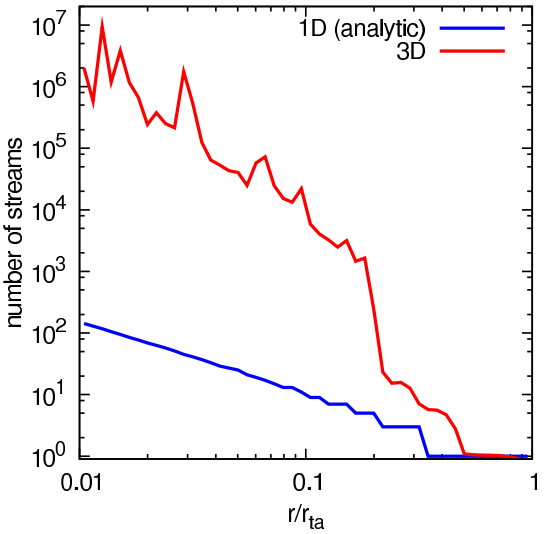

Figure 12. Number of streams as a function of radius for the 1D similarity solution (blue) and the 3D simulation (red). In 3D. stream stretching reduces individual stream density more efficiently than in 1D, leading to a larger number of streams at each radius. For the 1D similarity case the number of streams in the FG solution is shown. In the 3D case we use the mean harmonic stream density of the particles in a set of logarithmic bins to estimate the number of streams (see text).

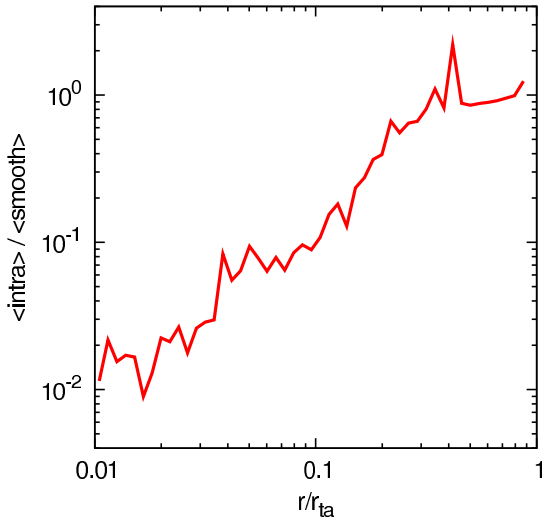

Figure 14. Local ratio of the intra-stream annihilation rate to the smoothed annihilation rate as a function of radius. The smoothed annihilation rate is calculated from an SPH-based density estimate using 64 neighbours. As expected, the strongest caustic contributions are found in the outer regions. Near 1% of the turnaround radius the contribution from caustics is at the percent level. This reflects the rapid dilution of stream densities in a 3D system.

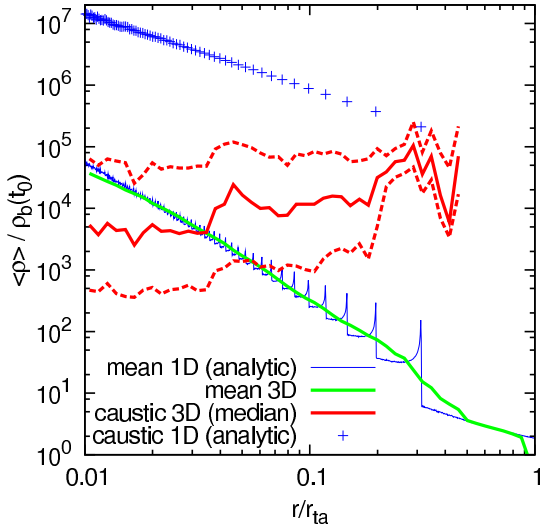

Figure 13. Densities at caustic passage as a function of radius and in units of the current mean cosmic density for the 1D similarity solution (blue crosses) and for the 3D simulation (red curves showing the median and quartiles at each radius). These caustic densities are compared to the mean density profiles of the two systems (blue curve for the 1D similarity solution, green curve for the 3D simulation). In 3D the outermost caustics are as dense as those found in 1D, reflecting the more rapid mixing in the three-dimensional system.

dian number of caustic passages experienced by particles in a set of logarithmic radial bins. The number is typically three to six times larger for the simulation than for the similarity solution. This is easily understood as reflecting the increased number of turning points along typical orbits. The overshoot in the regions just inside the outermost caustic is related to the feature in phase-space seen in Fig. 8.

Since the mean density profiles are similar in the 3D and 1D cases, the lower stream densities in 3D lead to a larger number of streams at each radius. Counting the number of streams in 1D is straightforward, given the similarity solution. In 3D we can estimate the number of streams crossing a given radial bin as a suitable average over the stream densities of the particles it contains $N_{\rm streams} \sim \rho(r)\ \langle 1/\rho_s \rangle_r$, where $\rho(r)$ is the mean mass density in the bin and $\langle 1/\rho_s \rangle_r$ is the average of the reciprocal of the stream densities of the particles. The comparison is shown in Fig. 12. The greatly enhanced mixing in 3D is clearly seen in this figure. At 1% of the turnaround radius there are of order 10^6 streams in the 3D simulation but only of order 100 in the FG solution. Estimates of the number of streams near the Sun based on 1D models (e.g. Natarajan & Sikivie 2005) give severe underestimates of the expectation in more realistic models.

In Fig. 13 we show as a function of radius the median and quartiles of the density at caustic crossing for all particles in the 3D simulation that crossed a caustic in the 0.014 Gyr immediately preceding t_0. For comparison, we also show the mean density profile of the halo in the 1D and 3D case. In the outer regions the density at caustic crossing is typically a thousand times the local mean halo density. Thus one might expect caustics to be visible in the halo annihilation signal at these radii. In the inner halo, however, the densities at caustic crossing do not rise as in the 1D similarity solution (also shown for comparison) but rather stay constant or even drop somewhat, Below $r/r_{\rm ta} = 0.03$ the median density at caustic crossing is smaller than the local mean halo density and one may expect caustics to play no significant role in the annihilation signal.

In the inner regions, stream and caustic densities are much lower in the 3D simulation than in the 1D similarity solution, but the number of caustics is only a few times greater. As a result less caustic-related annihilation radiation is expected in the 3D case. In Fig.14 we show the ratio of intra-stream annihilation rate (i.e. the contribution from particles which are both part of the same stream) to the annihilation rate estimated from the smoothed total density. The latter is calculated by SPH techniques using 64 neighbours.

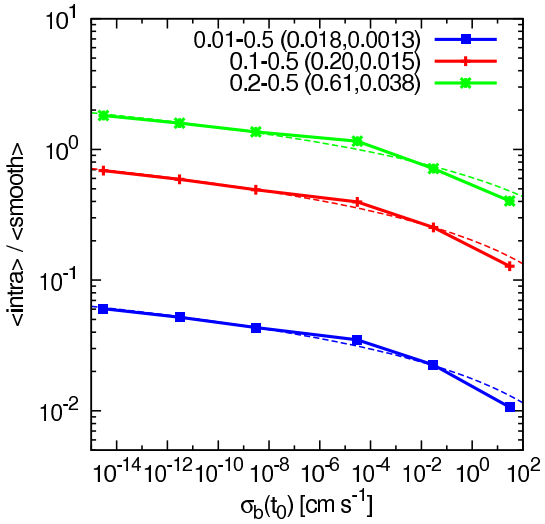

Figure 15. Intra-stream contribution to the annihilation rate as a function of the present-day neutralino velocity dispersion in unclustered regions and for different radial ranges (distinguished by colour; see legend which gives the range in units of the turnaround radius). The caustic contribution dominates and increases only logarithmically with decreasing dispersion. The dashed lines are analytic fits to the numerical results using Eq. (7). The fitting parameters a, b are shown in the brackets in the legend.

Fig.14 shows that intra-stream annihilation (which is dominated by caustic annihilation) does not contribute strongly to the overall annihilation rate. This is especially true in the inner region of the halo, where the stream and caustic densities are strongly suppressed. We find that for the radial interval $r/r_{\rm ta} \in (0.01, 0.5)$ the intra-stream contribution is only 4%. If we focus on the outer regions we find a contribution of 24% for $r/r_{\rm ta} \in (0.1, 0.5)$ and 64% for $r/r_{\rm ta} \in (0.2, 0.5)$, the range where the particles turn around for the second time and produce the outermost caustics.

All the above results are based on a present-day neutralino velocity dispersion of $\sigma_{\rm b}(t_0) = 0.03$ cm/s in unclustered regions. The dominant contribution to the intra-stream annihilation rate comes from caustics if the velocity dispersion is small. The densities of caustics are proportional to $1/\sqrt{\sigma_{\rm b}}$, and so are easily scaled to an arbitrary velocity dispersion. In Fig. 15 we show the radial dependence of the intra-stream annihilation rate for a range of velocity dispersions $\sigma_{\rm b}(t_0)$. These results are based on 64^3 particle simulations with a softening length of $0.01\ r_{\rm ta}$. We plot the intra-stream contribution for three different radial ranges as a function of velocity dispersion. A good analytic fit to the numerical results (dashed lines) for each radial interval is given by

$$\frac{\langle \rm intra \rangle}{\langle \rm smooth \rangle} = a + b\ \log \frac{1\ \rm cm/s}{\sigma_b(t_0)}. \qquad (7)$$

We note that this logarithmic behaviour is expected given the analysis of WV and the fact that the dominant contribution comes from caustics. From Fig. 15 we conclude that decreasing the velocity dispersion by 10 orders of magnitude from our standard value only increases the intra-stream annihilation contribution by a factor of about two. In the outer part of the halo, this would boost the total annihilation rate by almost a factor of two for the lowest dispersion shown in the plot, but in the inner regions the caustic contributions would still be small. For a typical neutralino with a mass around $100\ \rm GeV\ c^{-2}$ we do not confirm the substantial boost factors claimed by Hogan (2001).

4 CONCLUSIONS

We have used the geodesic deviation equation formalism recently developed by Vogelsberger et al. (2008) together with the fully general treatment of annihilation in caustics by White & Vogelsberger (2009) to understand how fine-grained phase-space structure affects the annihilation radiation from the dark matter haloes that form from self-similar, spherical initial conditions. Such objects do not evolve according to the well-known one-dimensional similarity solutions. Rather, they turn into highly elongated bars as a result of the radial orbit instability. These bars have mean mass density and total velocity dispersion profiles which are very similar to those of the relevant similarity solutions, but the loss of spherical symmetry results in orbits that fill a 3D volume and along which the stream density typically decreases as $1/t^3$ rather than as $1/t$ as in the similarity solution. At any given time, typical stream densities decrease slightly towards the centre of our simulation, whereas they increase strongly in the similarity solution. As a consequence, there are many more streams in the inner regions of the simulation than in the similarity solution. At 1% of the turnaround radius we find $\sim 10^6$ streams in the simulation but only about 100 in the similarity solution. This contradicts recent claims that the number of streams near the Sun should be relatively small (e.g. Natarajan & Sikivie 2005) but agrees with the estimates of Helmi et al. (2003). The number of caustics changes much less dramatically between the two cases, with a few times more caustics in the inner regions of the simulation as in the comparable region of the similarity solution. This is as expected given the higher dimensionality of the simulation orbits.

The impact of caustics on the annihilation signal depends on their density and number. Caustic densities in our simulation are much smaller than in the similarity solution, but their abundance is only modestly increased. As a result, annihilation radiation from caustics is less important in 3D than in 1D. For example, within the radial range $r/r_{\rm ta} \in (0.01, 0.5)$ caustics contribute only 4% of the smooth annihilation signal. If we focus on the region containing the outermost caustics, $r/r_{\rm ta} \in (0.2, 0.5)$, this ratio is 64%, similar to that predicted by the similarity solution. Decreasing the velocity dispersion by 10 orders of magnitude from our standard value only increases the caustic contribution to the annihilation luminosity by a factor of about two. This is because the annihilation signal from caustic crossing depends only logarithmically on the dark matter velocity dispersion.

Our results are based on a simplified and unrealistic halo formation model. However, haloes growing from ΛCDM initial conditions are expected to mix even more efficiently, because the fully three-dimensional character of orbits is retained and small-scale structure is expected to enhance the stretching of the phase-space sheets and hence to result in even greater dilution of their 3-densities. Thus, caustics will likely be less important in the ΛCDM case than in the simple isolated halo model discussed in the present paper. This strengthens our conclusion that 1D similarity solutions are inadequate and misleading models for the evolution of the fine-grained structure of real dark matter haloes. This applies not only to the original FG solutions but also to spherically symmetric generalisations of them (e.g. Sikivie et al. 1995, 1997; Duffy & Sikivie 2008). These still give qualitatively incorrect predictions for the dynamical dilution of stream densities. The inclusion of baryons would affect the dynamics of the dark matter in the inner halo, but would neither change the dimensionality of the orbits nor substantially modify their characteristic timescales. Thus no qualitative changes in behaviour are expected. The somewhat shorter orbital

timescales produced by compression of the inner halo are likely, if anything, to accelerate mixing. Our general conclusions should thus be unaffected.

In our analysis we have assumed that the annihilation cross-section does not depend on the dark matter phase-space structure. In general this assumption is correct, but it is altered for a recently proposed mechanisms to enhance the annihilation radiation. There an attractive force between dark matter particles is assumed in a way that the annihilation cross-section can be increased by the well-known process of Sommerfeld enhancement (e.g. Sommerfeld 1931; Hisano et al. 2004, 2005; Cirelli et al. 2007; Arkani-Hamed et al. 2009; Lattanzi & Silk 2009). This effect leads to an increase in the annihilation cross-section that, away from resonances and before saturation takes place, scales like $1/v$, where v is the particle encounter velocity. Therefore, the effect enhances the annihilation radiation in low velocity dispersion regions like subhaloes (e.g. Bovy 2009). In that case the annihilation radiation in caustics will be strongly suppressed, because the velocity dispersion in caustics is very high due to their high real-space density and conservation of phase-space density according to Liouville's theorem. In such a scenario fine-grained streams will be Sommerfeld enhanced because they have a very low velocity dispersion and particle encounter velocities are small in CDM streams. This implies that the intra-stream annihilation taking into account Sommerfeld enhancement will not be dominated by caustics anymore as it is the case for a phase-space independent particle physics prefactor assumed in the analysis above. We will discuss this in more detail in a future paper.

REFERENCES

Antonov V. A., 1973, in Dynamics of Galaxies and Star Clusters On the instability of stationary spherical models with merely radial motions, pp 139–143

Arkani-Hamed N., Finkbeiner D. P., Slatyer T. R., Weiner N., 2009, Phys. Rev. D, 79, 015014

Barnes J., 1985, in Goodman J., Hut P., eds, Dynamics of Star Clusters Vol. 113 of IAU Symposium, Dynamical instabilities in spherical stellar systems. pp 297–299

Bellovary J. M., Dalcanton J. J., Babul A., Quinn T. R., Maas R. W., Austin C. G., Williams L. L. R., Barnes E. I., 2008, ApJ, 685, 739

Bertschinger E., 1985, ApJS, 58, 39

Bovy J., 2009, Phys. Rev. D, 79, 083539

Carpintero D. D., Muzzio J. C., 1995, ApJ, 440, 5

Cirelli M., Strumia A., Tamburini M., 2007, Nuclear Physics B, 787, 152

Diemand J., Kuhlen M., Madau P., Zemp M., Moore B., Potter D., Stadel J., 2008, Nature, 454, 735

Duffy L. D., Sikivie P., 2008, Phys. Rev. D, 78, 063508

Fillmore J. A., Goldreich P., 1984, ApJ, 281, 1

Gavazzi R., Mohayaee R., Fort B., 2006, A&A, 445, 43

Helmi A., White S. D. M., 1999, MNRAS, 307, 495

Helmi A., White S. D. M., Springel V., 2003, MNRAS, 339, 834

Henriksen R. N., Widrow L. M., 1997, Physical Review Letters, 78, 3426

Henriksen R. N., Widrow L. M., 1999, MNRAS, 302, 321

Hisano J., Matsumoto S., Nojiri M. M., 2004, Physical Review Letters, 92, 031303

Hisano J., Matsumoto S., Nojiri M. M., Saito O., 2005, Phys. Rev. D, 71, 063528

Hogan C. J., 2001, Phys. Rev. D, 64, 063515

Kotok E. V., Shandarin S. F., 1987, Soviet Astronomy, 31, 600

Lattanzi M., Silk J., 2009, Phys. Rev. D, 79, 083523

MacMillan J. D., Widrow L. M., Henriksen R. N., 2006, ApJ, 653, 43

Merritt D., 1999, PASP, 111, 129

Mohayaee R., Salati P., 2008, MNRAS, 390, 1297

Mohayaee R., Shandarin S., Silk J., 2007, Journal of Cosmology and Astro-Particle Physics, 5, 15

Mohayaee R., Shandarin S. F., 2006, MNRAS, 366, 1217

Natarajan A., 2007, Phys. Rev. D, 75, 123514

Natarajan A., Sikivie P., 2005, Phys. Rev. D, 72, 083513

Natarajan A., Sikivie P., 2006, Phys. Rev. D, 73, 023510

Nusser A., 2001, MNRAS, 325, 1397

Polyachenko V. L., 1981, Soviet Astronomy Letters, 7, 79

Sikivie P., 1998, Physics Letters B, 432, 139

Sikivie P., Tkachev I. I., Wang Y., 1995, Physical Review Letters, 75, 2911

Sikivie P., Tkachev I. I., Wang Y., 1997, Phys. Rev. D, 56, 1863

Sommerfeld A., 1931, Annalen der Physik, 403, 257

Springel V., 2005, MNRAS, 364, 1105

Springel V., Wang J., Vogelsberger M., Ludlow A., Jenkins A., Helmi A., Navarro J. F., Frenk C. S., White S. D. M., 2008, MNRAS, 391, 1685

Vogelsberger M., White S. D. M., Helmi A., Springel V., 2008, MNRAS, 385, 236

White S. D. M., Vogelsberger M., 2009, MNRAS, 392, 281

White S. D. M., Zaritsky D., 1992, ApJ, 394, 1

Zeldovich Y. B., Shandarin S. F., 1982, Sov. Astron. Lett., 8, 139

Zemp M., Diemand J., Kuhlen M., Madau P., Moore B., Potter D., Stadel J., Widrow L., 2009, MNRAS, 394, 641

APPENDIX A: GDE ANALYSIS OF THE 1D SELF-SIMILAR INFALL

We start from the equations of motion in the similarity variables $\lambda = r/r_{\rm ta}$ and $\tau = t/t_{\rm ta}$ introduced by FG ($t_{\rm ta}$ and $r_{\rm ta}$ are the turnaround time and radius of the particle under consideration)

$$\frac{{\rm d}^2\lambda}{{\rm d}\tau^2} = -\frac{2}{9}\left(\frac{3\pi}{4}\right)^2 \frac{\tau^{2/(3\epsilon)}}{\lambda^2}\mathcal{M}\left(\frac{\lambda}{\Lambda}\right), \qquad \text{(A1)}$$

where $\mathcal{M}$ is the dimensionless enclosed mass (see Eq. (4)), $\Lambda(\tau) = \tau^{\Theta}$ and $\Theta = 2/3 + 2/(9\epsilon)$. The initial conditions are $\lambda(1) = 1$ and ${\rm d}\lambda/{\rm d}\tau(1) = 0$, corresponding to the Lagrangian physical coordinates $q = r_{\rm ta}$ (radial distance) and $p = 0$ (radial velocity). The physical distortion tensor (see VWHS) can be related to the equivalent tensor expressed in terms of similarity variables through

$$D_{rq} = D_{\lambda\lambda_0}, \qquad D_{rp} = \frac{t}{\tau}D_{\lambda\lambda_0'},$$
$$D_{vq} = \frac{\tau}{t}D_{\lambda'\lambda_0}, \qquad D_{vp} = D_{\lambda'\lambda_0'}. \qquad \text{(A2)}$$

$D_{\lambda\lambda_0}$ and $D_{\lambda\lambda_0'}$ are two solutions to the the geodesic deviation equation in two-dimensional phase-space

$$\widetilde{D}'' = \frac{2}{9}\left(\frac{3\pi}{4}\right)^2 \tau^{2/(3\epsilon)}\left(\frac{2\mathcal{M}(\lambda)}{\lambda^3} - \frac{1}{\lambda^2}\frac{{\rm d}\mathcal{M}(\lambda)}{{\rm d}\lambda}\right)\widetilde{D}, \qquad \text{(A3)}$$

where $\widetilde{D} = D_{\lambda\lambda_0}$ or $\widetilde{D} = D_{\lambda\lambda_0'}$. The initial conditions are $\widetilde{D}(1) = 1, \widetilde{D}'(1) = 0$ for $D_{\lambda\lambda_0}$ and $\widetilde{D}(1) = 0, \widetilde{D}'(1) = 1$ for

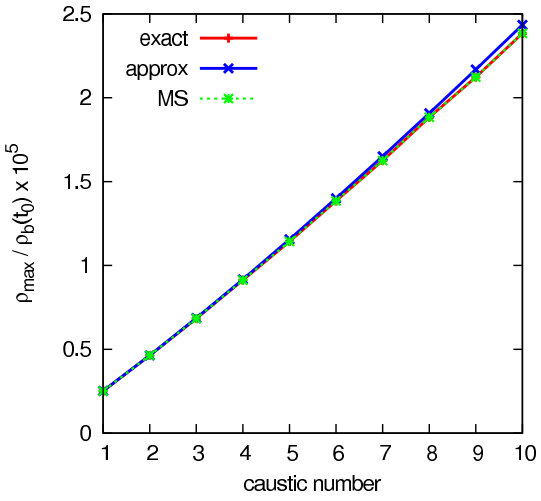

Figure A1. Caustic density for the 1D similarity solution with $\epsilon = 1$. Red shows the densities using the exact $\partial^2 A/\partial v^2$ values from the solution, while the blue line shows the result from using the Galilean-invariant estimate discussed in the text. The green line is the result obtained by MS. The agreement of our results with those presented in MS shows that our different approaches to calculating densities at caustic passage give the same result.

$D_{\lambda\lambda'_0}$. The two missing tensor components are given by τ derivatives of $\widetilde{D}$. To determine the stream density as a function of τ we need the linear and second order terms

$$\frac{\partial A}{\partial v} = D_{\lambda\lambda_0} + \left(\frac{3\pi}{4}\right)^2 \frac{1}{3+1/\epsilon} D_{\lambda\lambda'_0},$$
$$\frac{\partial^2 A}{\partial v^2} = -t_{\rm ta} D_{\lambda\lambda'_0} \frac{\tau^{1+\Theta}}{r_{\rm ta}\Theta^2}\left((1-\Theta)\frac{{\rm d}\lambda}{{\rm d}\tau} + \tau\frac{{\rm d}^2\lambda}{{\rm d}\tau^2}\right), \quad \text{(A4)}$$

where $A(q,p) = p - V(q)$ and $r_{\rm ta}$ is the current turnaround radius. The stream density for a particle is the integral of the phase-space density over velocity space (see WV). Using the linear and second order results from above, this yields

$$\rho_s(\tau) = \frac{\rho_0\, e^\beta K_{1/4}(\beta)}{\lambda^2\sqrt{2\pi}\sigma_0}\left|\frac{\partial A}{\partial v}\Big/\frac{\partial^2 A}{\partial v^2}\right|, \; \beta = \left(\frac{\partial A}{\partial v}\right)^4\Big/\left(2\frac{\partial^2 A}{\partial v^2}\sigma_0\right)^2, \quad \text{(A5)}$$

for the central particle of a phase-sheet, where the factor $1/\lambda^2$ is due to the $1/(s_1 s_2)$ prefactor associated with the stretching of the non-caustic directions and $K_{1/4}$ is the modified Bessel function. The intra-stream annihilation rate contribution of a small mass element ${\rm d}M_i$ is given by ${\rm d}P_{\rm intra} = \rho_s(\tau)\,{\rm d}M_i$. Integrating over all mass elements yields the total intra-stream annihilation rate

$$P_{\rm intra} = \frac{2M_{\rm ta}}{3\epsilon}\int_1^\infty \frac{{\rm d}\tau}{\tau^{1+2/(3\epsilon)}}\rho_s(\tau), \quad \text{(A6)}$$

where $M_{\rm ta}$ is the turnaround mass.

In Fig. A1 we show the densities of the first 10 caustics calculated using this GDE approach. For comparison to previous work we have chosen $\epsilon = 1$ and $r_{\rm ta}(t_0) = 1400$ kpc. We used both the exact second-order term of the similarity solution and an estimate based on Galilean-invariant first-order quantities (see WV)

$$\left|\frac{\partial^2 A}{\partial v^2}\right| \sim \left|\frac{\partial A}{\partial x}\right|\frac{1}{|a|} = \left|\frac{\partial v}{\partial q}\right|\frac{1}{|a|}. \quad \text{(A7)}$$

The green dashed line shows the results of MS. All results show good agreement. In Fig. A2 (top panel) we show the caustic density for velocity dispersions ranging from 10^2 cm/s down to 10^{-6} cm/s.

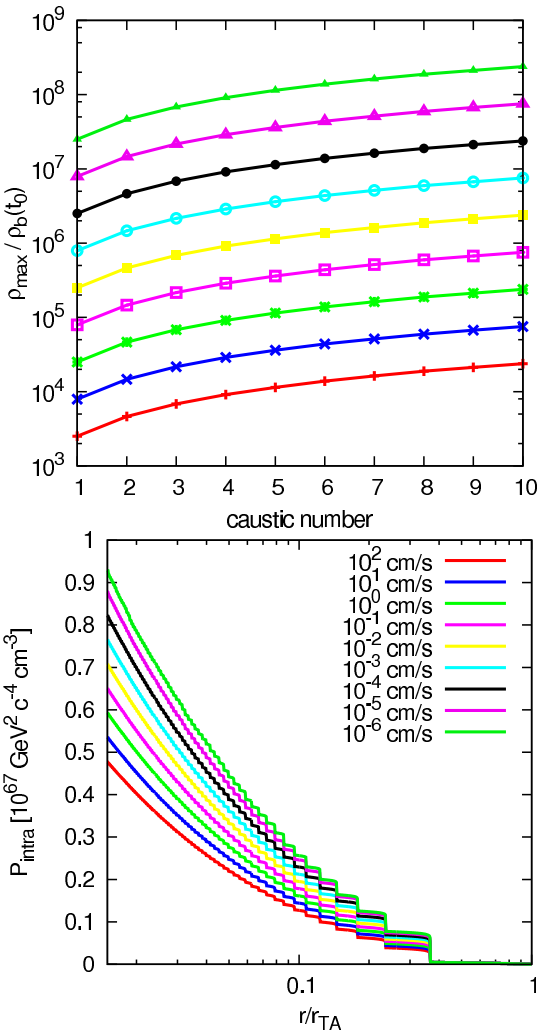

Figure A2. Top panel: Density at caustic crossing in units of the cosmic mean density and for different velocity dispersions. Density scales like $1/\sqrt{\sigma_b}$ at each caustic. The dispersions differ by factors of 10 so that the caustic densities differ by factors of $\sqrt{10}$. Bottom panel: Cumulative intra-stream annihilation rate counted outside to inside for the same set of dispersions. Although the dispersions change by 8 orders of magnitude, the intra-stream annihilation rate only changes by a factor of 2 over the radial range shown. This is due to the logarithmic $\sigma_{\rm b}$ dependence of the annihilation contribution from caustic crossing.

The maximum density scales as $1/\sqrt{\sigma_b}$ (see WV) so that all lines in this plot are separated by a factor of $\sqrt{10}$. The bottom panel shows the corresponding cumulative intra-stream annihilation rate (outside to inside). Although the dispersion varies over eight orders of magnitude, the total intra-stream contribution only changes by about a factor of 2. This is a consequence of the logarithmic divergence of the intra-stream annihilation luminosity near caustics (see WV).